Electronic Supplementary Material (ESI) for Journal of Materials Chemistry A.

Supplementary Information

Interlayer carrier high-speed conductive channel and excellent electrical transport performance of multilayer films

Shaoqiu Ke,[1, a] Tiantian Chen,[1, a] Xiaolei Nie,[a,*] Xiaoling Ai,[a] Tonglu Huang,[a] Haojun Zhang,[a] Longzhou Li,[a] Wenjie Xu,[a] Chengshan Liu,[a] Wanting Zhu,[a] Ping Wei,[a, b] Danqi He,[a] Wenyu Zhao,[a,*] Qingjie Zhang[a]

[a] *State Key Laboratory of Advanced Technology for Materials Synthesis and Processing, Wuhan University of Technology, Wuhan 430070, China*

[b] *Nanostructure research center, Wuhan University of Technology, Wuhan 430070, China*

[*] Corresponding authors: W. Zhao (wyzhao@whut.edu.cn) X. Nie (xiaoleinie@whut.edu.cn)

S1. Experimental section

Materials

Diglycidyl ether of bisphenol-F was purchased from NanYa Electronic Material (Kunshan) Co., Ltd. (China). Methylhexahydrophthalic anhydride ($C_9H_{12}O_3$, 98%) and Anhydrous ethanol (C_2H_6O, 99.7%) were obtained from Sinopharm Chemical Reagent Co., Ltd. (China). 2-Ethyl-4-methylimidazole ($C_6H_{10}N_2$, 96%), Butyl glycidyl ether ($C_7H_{14}O_2$, 98%) and Iron powder (Fe, 99.9%, about 100 nm) were obtained from the Aladdin Reagent (Shanghai) Co., Ltd. (China). The commercial p-type $Bi_{0.5}Sb_{1.5}Te_3$ (BST) ingots were purchased from Guangdong Fuxin Technology Co., Ltd. (China). Polyimide film (PI, thickness is 0.25 mm and 0.05 mm, respectively) was supplied by Shenzhen Golden Green Leaf Electronic Material Co., Ltd. (China). Polyimide film (PI, thickness is 0.125 mm) was supplied by Dupont (USA). All reagents were used as received.

Sample preparation

Preparation of BST/epoxy paste: The printable BST/epoxy paste were prepared with BST powder, epoxy resin, hardener, catalyst and reactive diluent as following steps. Firstly, BST ingots were manually crushed and screened (120 meshes) to obtain BST powders. Then a series of flake-like shape BST powders were prepared with a planetary ball mill apparatus. Next, BST powders, Diglycidyl ether of bisphenol-F (epoxy resin), Methylhexahydrophthalic anhydride (hardener), 2-Ethyl-4-methylimidazole (catalyst) and Butyl glycidyl ether (reactive diluent) were blended with a mechanical stirrer and then ultrasonically dispersed to obtain BST/epoxy paste. The weight ratio of powders-to-epoxy-to-hardener-to-catalyst-to-diluent was 100:6:5:1.2:18.

Preparation of Fe-NPs/epoxy paste: The printable Fe nanoparticles (Fe-NPs)/epoxy paste were prepared with Fe-NPs powder, epoxy resin, hardener, catalyst and reactive diluent as following steps. The Fe-NPs powders, Diglycidyl ether of bisphenol-F (epoxy resin), Methylhexahydrophthalic anhydride (hardener), 2-Ethyl-4-methylimidazole (catalyst) and Butyl glycidyl ether (reactive diluent) were blended with a mechanical stirrer and then ultrasonically dispersed to obtain Fe-NPs/epoxy paste. The weight ratio of powders-to-epoxy-to-hardener-to-catalyst-to-diluent was 100:20:17:4:50.

Preparation of BST/xFe-BST epoxy multilayer films: The BST/epoxy paste and Fe-NPs/epoxy paste named as Slurries 1 and 2, respectively. Firstly, the Slurries 1 were deposited onto the polyimide (PI) substrates with about 125 μm in thickness via screen-printing, and then the films were dried at 373 K for 1 h to obtain the dry films 1. Secondly, the Slurries 2 were deposited onto the upper surface of the dry films 1 via screen-printing, and then the films were dried at 373 K for 1 h to obtain the dry films 2. The Slurries 1 were deposited onto the upper surface of the dry films 2 via screen-printing, and then the films were dried at 373 K for 1 h. Thirdly, the BST/*x*Fe-BST epoxy multilayer wet films with x layers of Fe-BST were obtained by repeating the second step to alternate screen-printing BST layer and Fe-NPs layer. Finally, the films were dried at 373 K for 3 h and then transferred into a homemade hot-pressing apparatus to have been cured at 573 K and 5 MPa to yield a series of BST/xFe-BST epoxy multilayer films. The single-leg devices were obtained by laser etching and welding electrode. These BST/xFe-BST epoxy multilayer films with layers $x = 0, 1, 2, 3$, and 4, were named as B(FB)0 (BST epoxy multilayer film), B(FB)1, B(FB)2, B(FB)3, and B(FB)4, respectively. The "B" stands for BST layer, "F" for Fe-NPs layer, and the "x" stands for the number of Fe-BST layers in the corresponding film. Moreover, to further reveal the effect of magnetic layers on the properties of the BST/xFe-BST epoxy multilayer films, a kind of extra samples were prepared in this work. It was the magnetic layers (Fe-NPs layers) located on the upper surface of the BST layers as a surface layer which was in contact with the air.

Fabrication of single-leg TE cooling device: The BST epoxy multilayer film and BST/xFe-BST epoxy multilayer films were etched into thermoelectric (TE) legs with 4 × 20 mm^2 by laser etching method. The Al/Cu/Ni layers as the electrodes were then precipitated on both ends of TE legs by vacuum evaporation technology reported elsewhere.[1] Finally, the Cu wires were welded on the electrodes to form single-leg TE cooling devices. Both ends of single-leg TE cooling devices were connected with the positive and negative poles of the power supply to measure the cooling performance.

Characterization

The phase constituents of BST/xFe-BST epoxy multilayer films were examined by powder X-ray diffraction (XRD, SmartLab, Rigaku Corporation, Tokyo, Japan) using Cu $K\alpha$ radiation ($\lambda = 0.154186$ nm) source. The cross-sectional morphologies were characterized by a field emission scanning electron microscope (FESEM, GeminiSEM 500, Carl Zeiss AG, Germany, Oberkochen). The microstructure of a polished cross section of the BST/xFe-BST epoxy multilayer films was characterized by electron probe micro-analyzer (EPMA, JXA-8230, Nippon Electronics Corporation, Tokyo, Japan). HRTEM samples were prepared using focused ion beam system (FIB, Helios NanoLab G3 UC, Thermo Fisher, Oregon, USA). The microstructures were observed by Thermo Fisher double aberration-corrected transmission electron microscopy with Cs-correctors (HRTEM, Titan Themis G2 60-300, Thermo Fisher, Oregon, USA) at 300 kV.

Properties measurement

The Seebeck coefficient α and electrical conductivity σ of all the samples were simultaneously measured using a standard four-probe method (CTA-3, Beijing Cryoall Science and Technology Co., Ltd., Beijing, China) in helium atmosphere from 300 K to 500 K. Uncertainties are ± 5-7% for σ and about ± 5% for α. The Hall coefficient (R_H)

was obtained via linearly fitting the Hall voltage versus magnetic field curves under different saturation magnetic field.[2] The traditional Var der Pauw Hall method is not applicable for the magnetic samples due to the anomalous Hall effect. To obtain the correct R_H of BST/xFe-BST epoxy multilayer films, a series of voltage ΔV_{xy} were firstly measured at 300 K with the Van der Pauw method under a fixed current (i =10 mA) and by varying the magnetic fields in the range of 0.1-1.5 Tesla (T). Where $\Delta V_{xy} = V_H + V_{aH}$, V_{H} is the normal Hall voltage induced B(FB)0 and $V_{aH} = i\mu_0 M(H) R_{aH}/d$ is the anomalous Hall voltage induced by Fe-NPs. The slope k_{H} of all samples were obtained via linearly fitting those ΔV_{xy} obtained from the saturation magnetic fields in the range of 0.6-1.5 T. Finally, the R_{H} of all the samples were calculated with the formula $R_{\mathrm{H}} = k_{\mathrm{H}}d/(i\mu_0)$, where d is the thickness of samples and μ_0 is the vacuum permeability ($\mu_0 = 4\pi\times10^{-7}\ \mathrm{V\cdot s\cdot A^{-1}\cdot m^{-1}}$). The carrier concentration (p) and carrier mobility (μ) were calculated according to the equations $p = 1/(eR_{\mathrm{H}})$ and $\mu=\sigma R_{\mathrm{H}}$, where e is the electron charge ($e = 1.6 \times 10^{-19}$ C). The magnetization versus magnetic field (M-H) curves were measured at room temperature with multi-VersaLab Vibrating Sample Magnetometer (VSM, VersaLab, Quantum Design INC., California, USA). The magnetoresistance curves were measured with multi-VersaLab Electrical Transport Option (ETO, VersaLab, Quantum Design INC., California, USA) under high magnetic fields at different temperatures. The cooling performance of single-leg flexible film devices were measured by a homemade apparatus. A direct power supply (Gwinstek, GPD-2303S) was used to provide the working current. Temperatures at both ends were detected by the high-precision T-type thermocouple (OMEGA Engineering INC.), and the data was recorded by the acquisition module and LabVIEW program. The bending tests were performed using a flexible material and device testing system (FlexTest-TM-L, Hunan Nasheng Electronic Technology Co., Ltd, Hunan, China).

The band gap E_{g} of a TE material may be approximately estimated with the equation of $E_{\mathrm{g}} = 2\ \alpha_{\max}\ T_{\max}$,[3] where $\alpha_{\max}$ is the maximum α in the whole temperature range of 300-500 K and $T_{\max}$ is the corresponding temperature to $\alpha_{\max}$. The E_{g} values of all the samples are listed in **Table 1**. The E_{g} of B(FB)0 is about 0.16 eV, which is well consistent with the previous reported value (0.165 eV).[4] The E_{g} values of all the BST/xFe-BST epoxy multilayer films decreased as the Fe-BST layer increases, indicating that the σ of all the BST/xFe-BST epoxy multilayer films could be significantly improved by intercalated Fe-NPs layer.

The in-plane thermal conductivity κ of all the samples was calculated with the formula $\kappa=\rho\cdot D\cdot C_{\mathrm{p}}$, where ρ is the density, D is the in-plane thermal diffusivity, and C_{p} is specific heat capacity. The in-plane thermal diffusivity D was measured by a laser flash method (LFA467, NETZSCH). It is hardly to separate the TE films from the substrates without destroying the TE films. Therefore, our samples with the PI substrate with about Φ 22 mm for measuring the in-plane D. The Lorenz number L values are calculated by this approximately satisfy equation[5]: $L=1.5+\exp[-|\alpha|/116]$, where L is in 10^{-8} WΩK^{-2} and α in μV/K.

S2. Microstructure of BST/*x*Fe-BST epoxy multilayer films

To reveal the connection between BST layer and Fe-NPs layer in the BST/*x*Fe-BST epoxy multilayer films, and to know whether Fe-NPs enters into BST layer, the distribution of BST and Fe-NPs in the fracture cross section of the films was observed by FESEM. **Fig. S1a-e** are the FESEM images of the fractured cross section of B(FB)0, B(FB)1, B(FB)2, B(FB)3, and B(FB)4, respectively. It can be seen that the fractured cross section in the middle of B(FB)0 is clean and free of any impurities. However, there is an obvious second phase in the fractured cross section around BST grains of BST/Fe-BST epoxy multilayer films, and the large amounts of Fe-NPs fill into the pores between two BST grains, which is beneficial to the excellent electrical transport properties. Moreover, it can be clearly seen that the layered BST particles in all samples have good orientation. Therefore, increasing the number of layers of Fe-BST has little effect on the orientation of BST grains in the BST/*x*Fe-BST epoxy multilayer films.

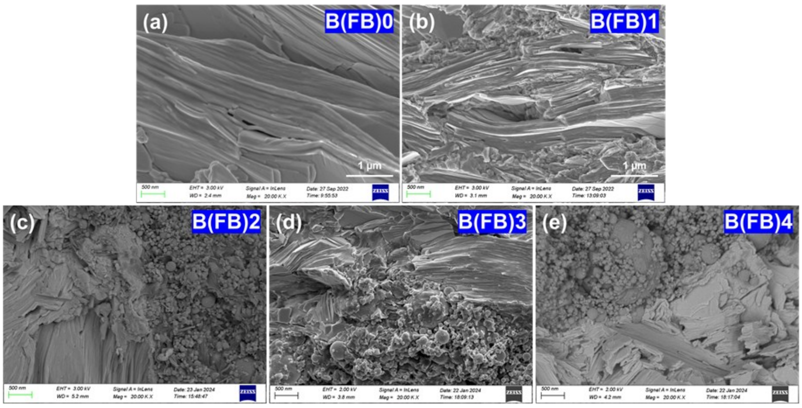

Figure 1. Microstructures from FESEM. The FESEM images of fractured cross section of (**a**) B(FB)0, (**b**) B(FB)1, (**c**) B(FB)2, (**d**) B(FB)3, and (**e**) B(FB)4.

We used SEM for element mapping (EDX) analysis of the BST/Fe interface (**Fig. S2**) to reveal pores/secondary phases formation. However, due to the resolution of the instrument, we can only see the pores, but cannot judge whether there is a secondary phase formation at the micrometer scale. To further reveal the existence of the secondary phase, we used HRTEM for EDX analysis of the BST/Fe interface. The HAADF-STEM image of the BST/Fe interface was shown in **Fig. S3a**. As can be seen from the mappings of Bi, Sb, Te, Fe and O (**Fig. S3b-f**), Fe element is enriching at some locations but no obvious enrichment of Bi, Sb and Te is observed at the same locations, indicating that Fe-NPs have not chemically reacted with Bi, Sb and Te elements. However, O element and Fe element are enriching at the same locations (**Fig. S3e-f**), indicating that partly Fe-NPs may have undergone the oxidation reaction with the oxygen from epoxy resin to form FeO compound. Therefore, secondary FeO compounds exist at the BST/Fe interface.

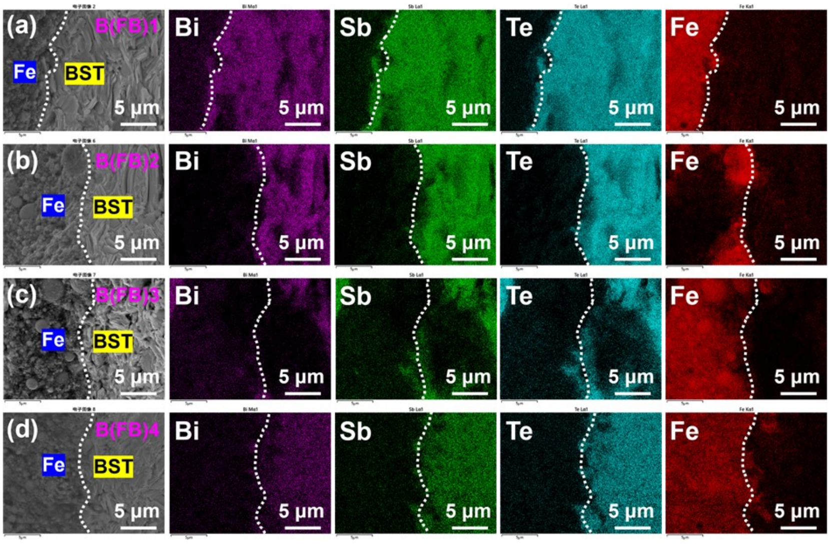

Figure 2. Microstructures from SEM. Backscattered electron images, corresponding elemental mappings of Bi, Sb, Te, and Fe element of (**a**) B(FB)1, (**b**) B(FB)2, (**c**) B(FB)3, and (**d**) B(FB)4.

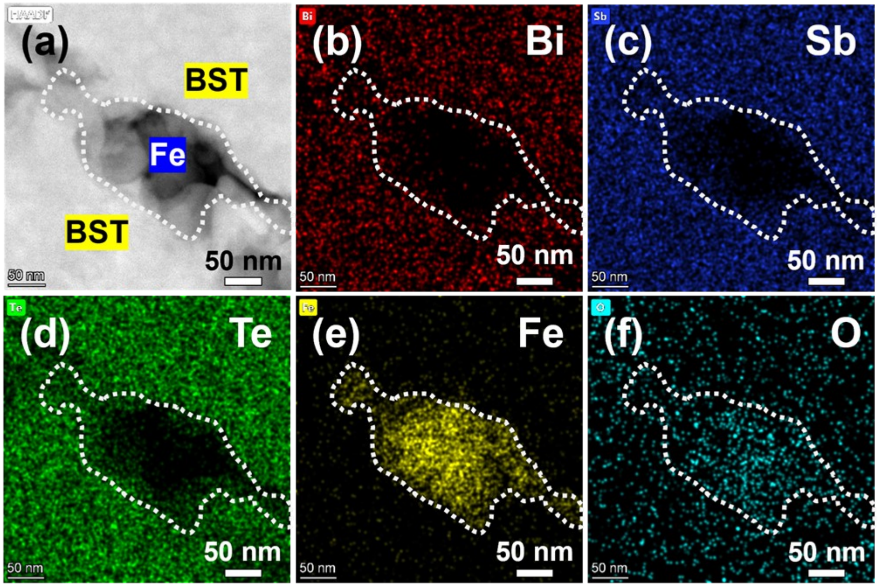

Figure 3. Microstructures from HRTEM. (**a**) HAADF-STEM image of the BST/Fe interface. Corresponding elemental mappings of Bi (**b**), Sb (**c**), Te (**d**), Fe (**e**), and O (**f**).

S3. Effect of location of Fe-NPs layer

To investigate the effect of location of Fe-NPs layer on the electrical transport performance for the BST/*x*Fe-BST epoxy multilayer films, a series of the BST/*x*Fe-BST epoxy multilayer films with different layers number (Fe-NPs layer or BST layer) were pretreated by first screen-printing the Fe-NPs layer, then alternately screen-printing the BST layer and the Fe-NPs layer, and then the films were prepared by hot-pressing curing process. The BST/*x*Fe-

BST epoxy multilayer film without Fe-NPs layer was named as B(FB)0. According to the screen-printing order of Fe-NPs layer and BST layer, the BST/*x*Fe-BST epoxy multilayer films were named FB, FBF, FBFB, respectively, where the “F” stands for Fe-NPs layer and “B” stands for BST layer. The dependence of σ, α and power factor $\alpha^2\sigma$ of the all samples are shown in **Fig. S4a-c**, respectively. The σ of all the samples in the range of 300-500 K is shown in **Fig. S4a**. Compared with the B(FB)0, the σ of FBF and FBFB was significantly decreased, the σ of FB was significantly increased. It was worth noting that when the Fe-NPs layer was used as the upper and lower layers of the film, the σ of the BST/*x*Fe-BST epoxy multilayer films deteriorates sharply, which indicates that the Fe-NPs layer was not suitable for both the upper and lower surface of the BST/*x*Fe-BST epoxy multilayer film (the upper surface of the film was in contact with the air). The α values of all samples is positive as shown in **Fig. S4b**, indicating that the carriers of all samples are holes. Compared with the B(FB)0, the α values of FBF and FBFB was significantly decreased, the α of FB was almost unchanged. Moreover, compared with the B(FB)0, the maximum α value of the BST/*x*Fe-BST epoxy multilayer films with Fe-NPs layers in the range of 300-500 K obviously moves to the low temperature region as shown in **Fig. S4b**, indicating that the Fe-NPs layer as the surface layer of BST/*x*Fe-BST epoxy multilayer films would promote the intrinsic excitation temperature of the BST/*x*Fe-BST epoxy multilayer films.

The power factor $\alpha^2\sigma$ values of all samples are calculated as shown in **Fig. S4c**. The $\alpha^2\sigma$ values of all samples decrease with increasing temperature. Compared with the B(FB)0, the $\alpha^2\sigma$ values of FBF and FBFB were significantly decreased. The maximum $\alpha^2\sigma$ values reaches 1.19 mW·K^{-2}·m^{-1} at 300 K for the FB. As a result, an Fe-NPs layer can optimize the electrical transport performance of the BST/*x*Fe-BST epoxy multilayer films under the BST layer as the surface layer of the films. At the same time, the Fe-NPs layer was not suitable for both the upper and lower surface of the BST/*x*Fe-BST epoxy multilayer films, otherwise it would deteriorate the electrical transport performance of the BST/*x*Fe-BST epoxy multilayer films.

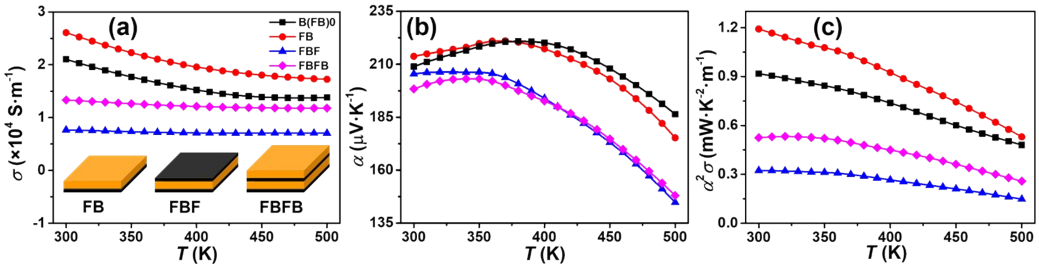

Figure 4. The effect of the location of Fe-NPs layer on the electrical transport performance for the BST/*x*Fe-BST epoxy multilayer films. Temperature dependence of (**a**) electrical conductivity, (**b**) Seebeck coefficient, and (**c**) power factor of the BST/*x*Fe-BST epoxy multilayer films.

S4. Effect of the mesh number of screen-printing

To investigate the effect of the mesh number of screen-printing on the electrical transport performance for the BST/*x*Fe-BST epoxy multilayer films, the B(FB)1 was pretreated by different mesh number of screen-printing. The temperature dependence of σ, α and power factor $\alpha^2\sigma$ of the B(FB)1 with different mesh number of screen-printing are shown in **Fig. S5a-c**, respectively. The σ decreases as mesh number of screen-printing increases as shown in **Fig. S5a**. The maximum σ reaches 5.69×10^4 S·m^{-1} at 300 K for the B(FB)1 under the 60 mesh of screen-printing. Regardless of the temperature, the magnitude of α is decreased as mesh number of screen-printing increases. At the room temperature, the maximum α reaches 200.63 μV·K^{-1} for the B(FB)1 under the 60 meshes of screen-printing. Moreover, the maximum α value of the all samples in the range of 300-500 K not shift as shown in **Fig. S5b**, indicating that the mesh number of screen-printing does not affect the intrinsic excitation temperature of the B(FB)1. The $\alpha^2\sigma$ values of all the samples are calculated as shown in **Fig. S5c**. The $\alpha^2\sigma$ values of all samples decrease with increasing temperature. At the same time, the $\alpha^2\sigma$ values decreases as mesh number of screen-printing increases. The maximum $\alpha^2\sigma$ value reaches 2.29 mW·K^{-2}·m^{-1} at 300 K for the B(FB)1 under the 60 meshes of screen-printing, increased by 1105% compared with that of the B(FB)1 under the 300 meshes of screen-printing. The results show that the smaller mesh number of screen printing will optimize the electrical transport performance of the BST/*x*Fe-BST epoxy multilayer films. Therefore, the optimal mesh number of screen printing for BST/*x*Fe-BST epoxy multilayer films preparation is 60.

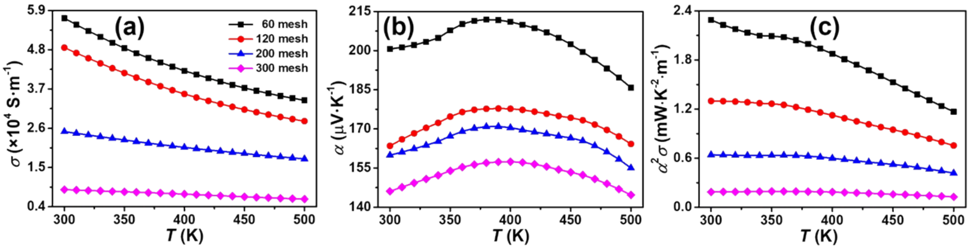

Figure S5. Effect of the mesh number of screen-printing on the electrical transport performance of B(FB)1. Temperature dependence of (**a**) electrical conductivity, (**b**) Seebeck coefficient and (**c**) power factor of the B(FB)1 with different mesh number of screen-printing.

S5. Effect of the epoxy resin

As we know, epoxy resin is insulating, and its presence will definitely worsen the electrical transport performance of the BST/*x*Fe-BST epoxy multilayer films. Moreover, the mass percentage of epoxy resin in the Fe-NPs layer is 47.64%, which is much higher than that of epoxy resin in the BST layer (23.20%). Therefore, with the increase of

x in BST/xFe-BST epoxy multilayer films (**Fig.5(b)**), the unit volume of the BST/xFe-BST epoxy multilayer films contain too much epoxy resin, and eventually the σ of the BST/xFe-BST epoxy multilayer films gradually decrease. To verify this view, we adjusted the epoxy resin content in Fe-NPs slurry from 47.64% in this study to 60.00% to prepare a BST/1Fe-BST epoxy multilayer film with higher epoxy resin per unit volume (named as Comparison sample 1), and its σ was shown in the **Fig. S6**. It can be seen that the σ of the BST/1Fe-BST epoxy multilayer film with higher epoxy resin was much lower than that of the B(BF)1. Moreover, the Fe-NPs layer without carrying epoxy resin by evaporation coating was embedded into the BST/1Fe-BST epoxy multilayer film (named as Comparison sample 2), and its σ was shown in the **Fig. S7**. It can be seen that when the Fe-NPs layer does not contain epoxy resin, the σ of the sample was higher than that of the B(FB)1. The above research results show that with the increase of x, the σ of the BST/xFe-BST epoxy multilayer films gradually decrease, which is mainly due to the excessive epoxy resin per unit volume contained in the film.

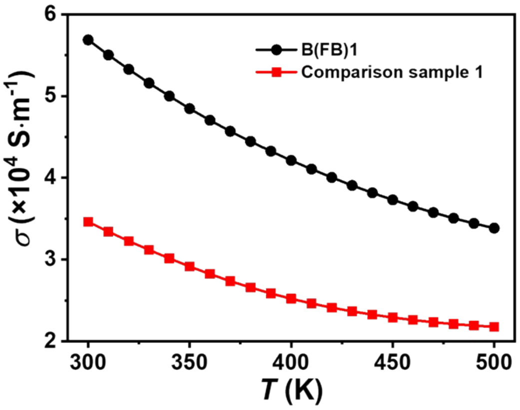

Figure S6. Temperature dependence of (**a**) electrical conductivity of the BST/1Fe-BST epoxy multilayer film with higher epoxy resin.

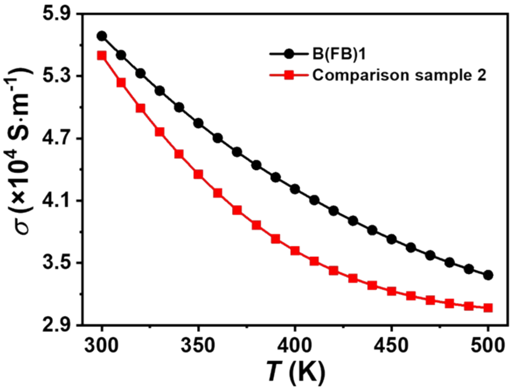

Figure S7. Temperature dependence of (**a**) electrical conductivity of the BST/1Fe-BST epoxy multilayer film, where the Fe-NPs layer without carrying epoxy resin prepared by evaporation coating.

S6. Thermal transport properties and *zT*

To further evaluate the in-plane thermal diffusivity *D* and *zT* value of all the samples, the in-plane *D* of BST/*x*Fe-BST epoxy multilayer films with the PI substrate was tested. The temperature dependence of the in-plane thermal conductivity κ, carrier thermal conductivity κ_{C}, lattice thermal conductivity κ_{L}, and *zT* of BST/*x*Fe-BST epoxy multilayer films with PI substrate were shown in **Fig. S8**, respectively. The κ of all samples first decreases and then increases with increasing temperature as shown in **Fig. S8a**. The decrease in κ is due to the increase of lattice vibration, and the increase in the κ is due to intrinsic excitation. The κ_{C} of all samples increases with increasing temperature due to the increased σ of all samples as shown in **Fig. S8b**. The κ_{C} of all the BST/Fe-BST epoxy multilayer films is significantly higher compared with that of the B(FB)0. This is attributed to the remarkable increase of σ of BST/Fe-BST epoxy multilayer films (**Fig. 5b**). The κ_{L} of all samples was calculated by the $\kappa_{\mathrm{L}} = \kappa - \kappa_{\mathrm{C}}$. The κ_{L} shows the same trend as κ with increasing temperature because the contribution of κ_{C} to κ is small as shown in **Fig. S8c**. The κ of the BST/Fe-BST epoxy multilayer films is significantly higher compared with that of the B(FB)0 as shown in **Fig. S8a**. The increase of the κ is attributed to the remarkable increase of the κ_{L} and κ_{C}. The increase of the κ_{L} is attributed to the large presence of Fe-NP. The calculated *zT* values, based on these measured σ, κ and α, increased induced by Fe-BST layer (**Fig. S8d**). The maximum *zT* is about 0.84 at 360 K for B(FB)1 with PI substrate, increased by 1.2 times as compared with that of B(FB)0 with PI substrate, which is more than all the *zT* values of organic/inorganic composite TE films reported by different groups as shown in **Fig. S9**.

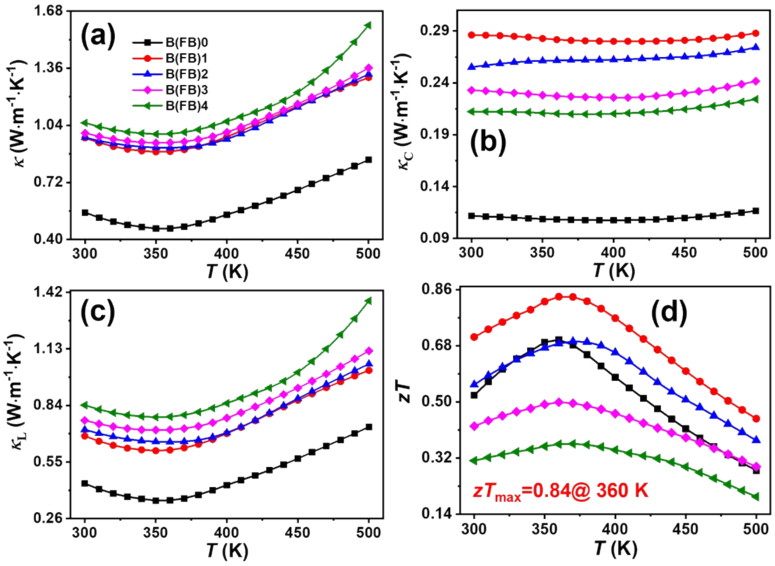

Figure S8. Thermal transport properties and *zT* of the films with PI substrate. Temperature dependence of (**a**) thermal conductivity κ, (**b**) carrier thermal conductivity κ_{C}, (**c**) lattice thermal conductivity κ_{L}, and (**d**) *zT* of the films with PI substrate.

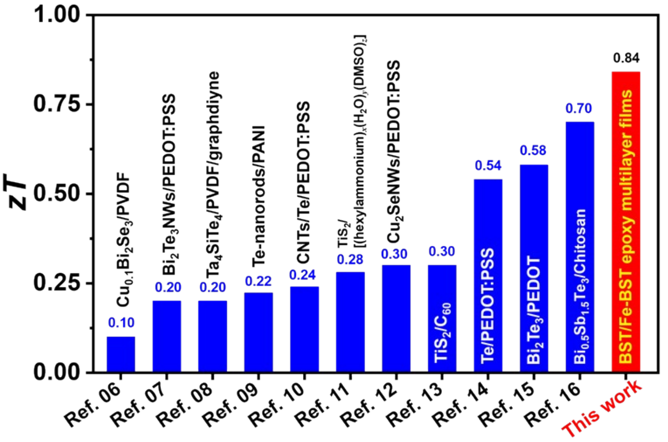

Figure S9. The maximum *zT* values of organic/inorganic composite TE films from different groups.[6-16]

S7. Flexibility testing of B(FB)1

The single-leg device of 4.0×20×0.092 mm^3 in size was fabricated with B(FB)1. The bending test was performed using a flexible material and device testing system (FlexTest-TM-L). The ratio of resistances (R/R_0) was recorded before and after bending test with different bending radius and cycle times. The initial internal resistance (R_0) of the device was 1.28 Ω. As shown in **Fig. S10a**, the internal resistance (R_0) was almost unchanged when the bending radius gradually decreased from 25 mm to 10 mm while it started to rapidly increase when the bending radius decreased from 10 mm to 5 mm. The TE leg was cracked when the bending radius was less than 10 mm. To further investigate the flexibility of the single-leg device, the R is measured during the cycling bending test under the condition of bending radius 10 mm. As shown in **Fig. S10b**, it is noteworthy that the change in R remains within 10% when the cycle times are less than 2000. These bending test results demonstrate the great application potential of flexible $Bi_{0.5}Sb_{1.5}Te_3$-based films.

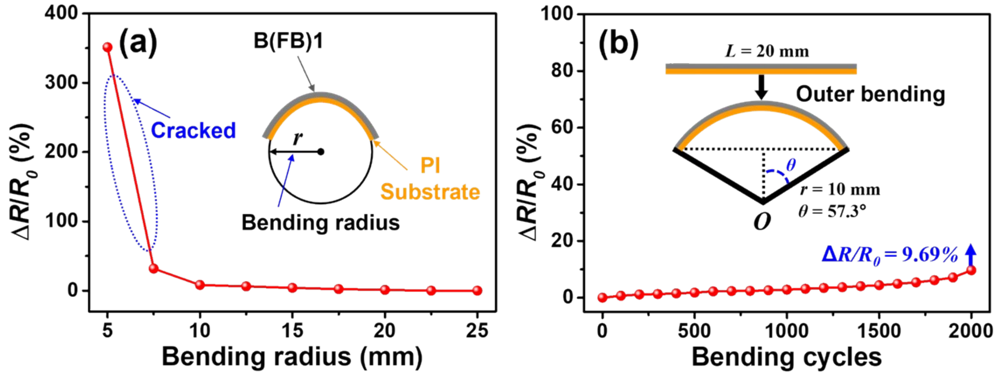

Figure S10. Flexibility testing of B(FB)1. (**a**) R/R_0 dependent bending radius, (**b**) R/R_0 dependent bending cycles.

S8. Negative magnetoresistances in BST/Fe-BST epoxy multilayer films

For the BST/Fe-BST epoxy multilayer films, the negative magnetoresistances (MR^-) mainly originates from the two factors as follows: One is the spin-dependent scattering (*SS*) due to the exchange interaction between the spin of conductive carriers and the localized magnetic moments of Fe-NPs. Such the exchange interaction makes the conductive carriers split into two half-bands with opposite spin directions and different relaxation time $\tau_\downarrow$ and $\tau_\uparrow$. [17] According to the suggestion by R. P. Khosla and J. R. Fischer, the MR_{SS}^- from *SS* effect may be given by [18]

$$MR_{SS}^- = \frac{\Delta\rho}{\rho_0} = -K_1 \ln(1 + K_2^2 H^2)$$

where K_1 and K_2 are constants. Another is the weak-localization scattering (*WL*) by the intrinsic and disordered defects such as lattice distortion induced by doped atoms, nanostructure of Fe-NPs, and organic-inorganic interfaces. The weak localization can cause a MR_{WL}^- when it is suppressed by applying an extra *H*. By extending the Kawabata's theory [19], the MR_{WL}^- from *WL* effect can be expressed as

$$MR_{WL}^- = \frac{\Delta\rho}{\rho_0} = -K_3 H^{1/2}$$

where K_3 is constant. Therefore, the total MR^- of BST/Fe-BST epoxy multilayer films can be expressed as

$$MR^- = MR_{SS}^- + MR_{WL}^- = -K_1 \ln(1 + K_2^2 H^2) - K_3 H^{1/2}$$

References

1. H. Zhou, X. Mu, W. Zhao, D. Tang, P. Wei, W. Zhu, X. Nie, Q. Zhang, *Nano Energy*, 2017, **40**, 274-281.
2. W. Y. Zhao, Z. Y. Liu, Z. G. Sun, Q. J. Zhang, P. Wei, X. Mu, H. Y. Zhou, C. C. Li, S. F. Ma, D. Q. He, P. X. Ji, W. T. Zhu, X. L. Nie, X. L. Su, X. F. Tang, B. G. Shen, X. L. Dong, J. H. Yang, Y. Liu, J. Shi, *Nature*, 2017, **549**, 247-251.
3. Z. M. Gibbs, H. S. Kim, H. Wang, G. J. Snyder, *Appl. Phys. Lett.*, 2015, **106**, 02211.
4. Y. L. Chen, J. G. Analytis, J.-H. Chu, Z. K. Liu, S.-K. Mo, X. L. Qi, H. J. Zhang, D. H. Lu, X. Dai, Z. Fang, S. C. Zhang, I. R. Fisher, Z. Hussain, Z.-X. Shen, *Science*, 2009, **325**, 178-181.
5. H.-S. Kim, Z. M. Gibbs, Y. L. Tang, H. Wang, G. J. Snyder. *APL Mater.*, 2015, **3**, 041506.
6. C. Dun, C. A. Hewitt, H. Huang, J. Xu, C. Zhou, W. Huang, Y. Cui, W. Zhou, Q. Jiang, D. L. Carroll, *Nano Energy*, 2015, **18**, 306.
7. W. S. Kim, G. Anoop, I. S. Jeong, H. J. Lee, H. B. Kim, S. H. Kim, G. W. Goo, H. Lee, H. J. Lee, C. Kim, J. H. Lee, B. S. Mun, J. W. Park, E. Lee, J. Y. Jo, *Nano Energy*, 2020, **67**, 104207.

8. S. Qu, C. Ming, P. Qiu, K. Xu, Q. Xu, Q. Yao, P. Lu, H. Zeng, X. Shi, L. Chen, *Energy Environ. Sci.*, 2021, **14**, 6586.
9. Y. Wang, S. M. Zhang, Y. Deng, *J. Mater. Chem. A*, 2016, **4**, 3554.
10. C. Liu, D. L. Shan, Z. H. Shen, G. K. Ren, W. Yue, Z. F. Zhou, J. Y. Li, D. Yi, J. L. Lan, L. Q. Chen, G. J. Snyder, Y. H. Lin, C. W. Nan, *Nano Energy*, 2021, **89**, 106380.
11. C. Wan, X. Gu, F. Dang, T. Itoh, Y. Wang, H. Sasaki, M. Kondo, K. Koga, K. Yabuki, G. J. Snyder, R. Yang, K. Koumoto, *Nat. Mater.*, 2015, **14**, 622.
12. Y. Lu, Y. Ding, Y. Qiu, K. Cai, Q. Yao, H. Song, L. Tong, J. He, L. Chen, *Acs Appl. Mater. Interfaces*, 2019, **11**, 12819.
13. L. Wang, Z. Zhang, L. Geng, T. Yuan, Y. Liu, J. Guo, L. Fang, J. Qiu, S. Wang, *Energy Environ. Sci.*, 2018, **11**, 1307.
14. L. Yang, M. P. Gordon, A. K. Menon, A. Bruefach, K. Haas, M. C. Scott, R. S. Prasher, J. J. Urban, *Sci. Adv.*, 2021, **7**, eabe6000.
15. L. Wang, Z. Zhang, Y. Liu, B. Wang, L. Fang, J. Qiu, K. Zhang, S. Wang, *Nat. Commun.*, 2018, **9**, 3817.
16. P. Banerjee, J. Huang, R. B. Ambade, E. Jang, M. Saeidi-Javash, Y. Zhang, D. Madan, *Nano Energy*, 2021, **89**, 106482.
17. M. Z. Maialle, *Phys. Rev. B*, 1996, **54**, 1967-1974.
18. R. P. Khosla, J. R. Fischer, *Phys. Rev. B*, 1970, **2**, 4084-4097.
19. A. Kawabata, *Solid State Commun.*, 1980, **34**, 431-432.